

Fundamental activity constraints lead to specific interpretations of the connectome

Jannis Schuecker^{1,*}, Maximilian Schmidt^{1,*}, Sacha J. van Albada¹, Markus Diesmann^{1,2,3}, and Moritz Helias¹

¹Institute of Neuroscience and Medicine (INM-6) and Institute for Advanced Simulation (IAS-6) and JARA BRAIN Institute I, Jülich Research Centre, Jülich, Germany

²Department of Psychiatry, Psychotherapy and Psychosomatics, Medical Faculty, RWTH Aachen University, Aachen, Germany

³Department of Physics, Faculty 1, RWTH Aachen University, Aachen, Germany

*Both authors contributed equally to this work.

arXiv:1509.03162v1 [q-bio.NC] 10 Sep 2015

Correspondence to: Jannis Schuecker
j.schuecker@fz-juelich.de

Abstract

The integration of incoming experimental data into coherent models of the brain is an increasing challenge of modern neuroscience. Such models provide a bridge between structure and activity, and identify the mechanisms giving rise to experimental observations. Nevertheless, structurally realistic network models of spiking neurons are necessarily under-constrained even if experimental data on brain connectivity are incorporated to the best of our knowledge. Guided by physiological observations, any model must therefore explore the parameter ranges within the uncertainty of the data. Based on simulation results alone, however, the mechanisms underlying stable and physiologically realistic activity often remain obscure. We here employ a mean-field reduction of the dynamics, which allows us to include activity constraints into the process of model construction. We shape the phase space of a multi-scale network model of primate visual cortex by systematically refining its connectivity. Fundamental constraints on the activity, i.e., prohibiting quiescence and requiring global stability, prove sufficient to obtain realistic layer- and area-specific activity. Only minimal adaptations of the structure are required, showing that the network operates close to an instability. The procedure identifies components of the network critical to its collective dynamics and creates hypotheses for structural data and future experiments.

Introduction

The neural wiring diagram, the connectome, is gradually being filled in through classical techniques combined with innovative quantitative analyses (Barone et al., 2000; Markov et al., 2014a,b) and new technologies (Wedeen et al., 2008; Axer et al., 2011). The connectivity between neurons is considered to shape both resting-state and task-related collective activity (Cole et al., 2014; Shen et al., 2015). For simple networks, clear relationships with the resulting activity are known, even analytically. For example, a dynamic balance between excitatory and inhibitory inputs in inhibition-dominated random networks leads to an asynchronous and irregular state (van Vreeswijk & Sompolinsky, 1996; Amit & Brunel, 1997a). Structures and mechanisms underlying large-scale interactions have been identified by means of dynamical models (Deco & Jirsa, 2012; Cabral et al., 2014) and graph theory (Markov et al., 2013; Goulas et al., 2014). Furthermore, the impact of local network structure on spike-time correlations is known in some detail (Ostojic et al., 2009; Pernice et al., 2011, 2012; Trousdale et al., 2012; Hu et al., 2013; Helias et al., 2013). Under certain conditions, there is a one-to-one mapping between correlations in neuronal network activity and effective connectivity, a measure that depends both on the network structure and on its activity (van Albada et al., 2015). Taken together, these studies imply that anatomy does not uniquely determine dynamics, but dynamical observations help constrain the underlying anatomy. Despite advances in the understanding of simple networks and mechanisms, a complete picture of the relationship between structure and dynamics remains elusive.

Fig. 1 visualizes the integrative loop between experiment, model, and theory that guides the investigation of structure and dynamics. In the traditional use of a network model, structural data from experimental studies determines the connectivity between model neurons. Combined with the specification of a particular single-neuron dynamics and synaptic interactions, simulations yield a certain network dynamics. There are two fundamental problems with this approach.

First, despite the impressive experimental progress in determining network parameters, any neural network model will be underdetermined, because of both the sheer complexity of the brain tissue and inevitable uncertainties in the data. For instance, counting synapses on a large scale presently takes a prohibitive amount of time, and no available technique allows determining precise synaptic weights for entire populations of neurons. Although it may be possible to quantify the full connectome of an individual in future, inter-individual variability will require modelers to express connectivity as connection probabilities or rules of self-organization if they want to learn about general principles of the brain. In modeling studies, the underdetermined parameters are usually tuned manually to achieve a satisfactory state of activity. For high-dimensional models, this approach becomes unfeasible due to the size of the parameter space.

Second, with a pure forward modeling approach, it is a priori unclear how parameters of the model influence its activity. In consequence, modifications cannot be performed in a targeted fashion, and it is difficult to find a minimal set of modifications necessary for aligning a model with the experimental activity data.

Overcoming these problems requires a shift of perspective. Instead of regarding the model exclusively in a forward manner, generating predicted activity from the underlying structure, we in addition consider the system in a reverse manner, predicting the structure necessary to explain the observed activity. Our theory, starting from a mean-field description, provides a direct link between structure and activity. In contrast to simulations, the theory is invertible, establishing a feedback path from the activity back to

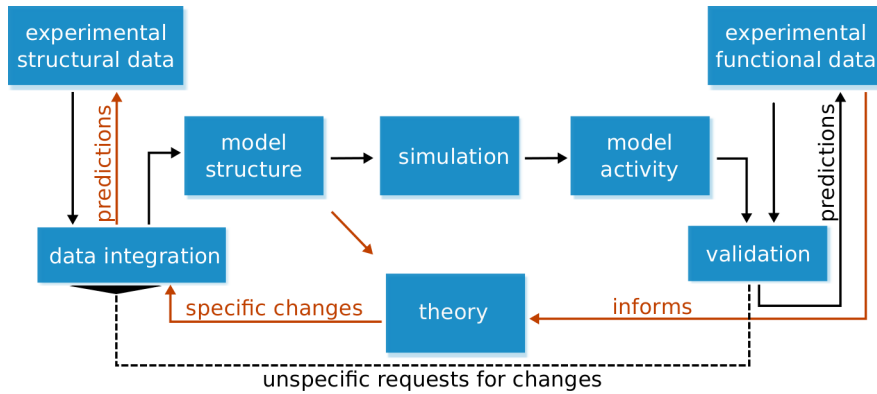


Figure 1: The integrative loop between experiment, model, and theory. Black arrows represent the classical forward modeling approach: Experimental structural data are integrated into a model structure, which gives rise to the activity via simulation. The model activity is compared to experimental functional data. The usual case of disagreement leads to the need to change the model definition. By experience and intuition the researcher identifies the parameters to be changed, proceeding in an iterative fashion. Once the model agrees well with a number of experimental findings, it may also generate predictions on the outcome of new experiments. Red arrows symbolize our new approach: informed by functional data, an analytical theory of the model identifies critical connections used to refine the integration of data into a consistent model structure and to generate predictions for anatomical studies.

structural data. Using the activity constraints from experiments, we exploit this invertibility to identify connections critical for the dynamics. This enables us to find a minimal set of modifications to the structure yielding a realistic set point of activity. The predicted alterations of the structure generate hypotheses on brain structure, thus feeding back to anatomical experiments.

Applying the method to a multi-scale network model of macaque visual cortex, we derive targeted modifications of a set of connections critical to its dynamics, bringing the model closer to experimental observations of cortical activity. Based on the global properties of the bistable phase space of the model, the method refines the model’s construction principles within experimental uncertainties and identifies the connections that decisively shape the dynamics. Preliminary results have been presented in abstract form (Schmidt et al., 2015).

Theory and Methods

Consider a neuronal network of leaky integrate-and-fire model neurons with exponentially decaying post-synaptic currents. In the diffusion approximation, the dynamics of the membrane potential V and synaptic current I_s is (Fourcaud & Brunel, 2002)

$$\begin{aligned} \tau_m \frac{dV}{dt} &= -V + I_s(t) \\ \tau_s \frac{dI_s}{dt} &= -I_s + \mu + \sigma \sqrt{\tau_m} \xi(t), \end{aligned} \quad (1)$$

where τ_m is the membrane time constant and τ_s the synaptic time constant, respectively. The membrane resistance has been absorbed into the definition of the current. The input spike trains are approximated by a current which fluctuates with variance σ^2 around the mean value μ where the noise fluctuations are drawn from a Gaussian process $\xi(t)$ satisfying $\langle \xi(t) \rangle = 0$ and $\langle \xi(t)\xi(t') \rangle = \delta(t - t')$. Whenever the membrane potential V crosses the threshold Θ , the neuron emits a spike and V is set to the reset potential V_r , where it is clamped during τ_r . In the models we consider, the neurons are structured into N populations interconnected with a connectivity matrix $\mathbf{W} = \mathbf{K} \otimes \mathbf{J}$, where K_{ij} is the number of incoming connections to a neuron in population i from population j , and J_{ij} is the efficacy of a single synapse in the respective connection. Here, \otimes denotes element-wise multiplication, also called the Hadamard product (see Cichocki et al., 2009, for a consistent set of symbols for operations on matrices). Additionally, each neuron is driven by K_{ext} Poisson sources with rate ν_{ext} and synaptic efficacy J_{ext} . All neurons in one population have identical parameters, so that we can describe the network activity in terms of population-averaged firing rates ν_i due to population-dependent input μ_i, σ_i determined by the connectivity. Using the Fokker-Planck formalism, the stationary firing rates for each population i are given by (Fourcaud &

$$\begin{aligned} \frac{1}{\nu_i} &= \tau_r + \tau_m \sqrt{\pi} \int \frac{\Theta - \mu_i(\mathbf{A})}{\sigma_i(\mathbf{A}) + \gamma \sqrt{\frac{\tau_s}{\tau_m}}} e^{x^2} (1 + \operatorname{erf}(x)) dx \\ &=: 1/\Phi_i(\boldsymbol{\nu}, \mathbf{A}) \end{aligned} \quad (2)$$

$$\mu_i(\mathbf{A}) = \tau_m \sum_j K_{ij} J_{ij} \nu_j + \tau_m K_{\text{ext}} J_{\text{ext}} \nu_{\text{ext}} \quad (3)$$

$$\sigma_i^2(\mathbf{A}) = \tau_m \sum_j K_{ij} J_{ij}^2 \nu_j + \tau_m K_{\text{ext}} J_{\text{ext}}^2 \nu_{\text{ext}}, \quad (4)$$

which is correct up to linear order in $\sqrt{\tau_s/\tau_m}$ and where $\gamma = |\zeta(1/2)|/\sqrt{2}$, with ζ denoting the Riemann zeta function (Abramowitz & Stegun, 1974). Here, \mathbf{A} is chosen from the set of model parameters $\{\mathbf{K}, \mathbf{J}, \nu_{\text{ext}}, \dots\}$. If \mathbf{A} is a matrix, we vectorize it by concatenating its rows and indicate this by lower case, i.e., $\mathbf{a} = (a_{00}, a_{01}, \dots, a_{0N}, a_{10}, \dots, a_{1N}, \dots, a_{NN}) = \operatorname{vec}(\mathbf{A}^T)^T$ (Magnus & Neudecker, 1995). If the chosen parameter is a scalar we denote it with a . We find the fixed points of (2) by solving the first-order differential equation (Wong & Wang, 2006)

$$\dot{\boldsymbol{\nu}} := \frac{d\boldsymbol{\nu}}{ds} = \boldsymbol{\Phi}(\boldsymbol{\nu}, \mathbf{A}) - \boldsymbol{\nu}, \quad (5)$$

using the classical fourth-order Runge-Kutta method (RK4) with step size $h = 0.01$ where s denotes a dimensionless pseudo-time. Note that (5) does not reflect the real time evolution of the population rates, but rather is a mathematical method to obtain the system's fixed points. In contrast to Wong & Wang (2006) we do not only search for stable fixed points, but use (5) also to obtain unstable attractors (cf. Results), an idea originating from a study of simple attractor networks by Amit & Brunel (1997b, esp. their Fig. 2 and Eq. (12)).

The non-linearity in the input-output relationship $\boldsymbol{\Phi}$ in combination with feedback connections in general can cause multi-stability in the network. In particular excitatory-excitatory loops cause the system (5) to exhibit multi-stable behavior in the stationary firing rates. Thus we require a method to control their influence on the phase space of the network. As an illustration we first study the mechanism using the simple network architecture depicted in Fig. 2A: a population of excitatory neurons is coupled to itself with indegree K and is driven by external Poisson sources with the same indegree $K_{\text{ext}} = K$ and rate ν_{ext} . All connections have identical synaptic weights J . An increase in the external drive shifts the input-output relationship $\boldsymbol{\Phi}(\boldsymbol{\nu}, a = \nu_{\text{ext}})$ of this one-dimensional system (Fig. 2C) to the left. The bifurcation diagram is shown in Fig. 2E: For low ν_{ext} there is only one fixed point with low activity (LA). When increasing ν_{ext} , a pair of fixed points of which one is stable and the other is unstable emerges via a saddle-node bifurcation, leading to a bistable system. The second stable fixed point exhibits high firing rates, denoted as the high-activity (HA) state. For even higher values of ν_{ext} , the LA state loses stability.

In the bistable situation, the initial condition of (5) determines which fixed point the system settles in. However, studying the behavior for a particular initial condition is of minor interest, since the actual spiking network is a stochastic system which fluctuates around the fixed points of the deterministic system defined by (5). Even if we knew that (5) would relax to the LA fixed point for one particular initial condition, this would not necessarily imply that this state is indefinitely stable. The global stability is determined by the size of the basin of attraction of the LA fixed point. Suppose that we want to increase the activity at the LA fixed point while maintaining its global stability. Then we can increase the external drive ν_{ext} while adjusting the internal connectivity K to preserve the basin of attraction.

The equilibria given by the zeros of the velocity $\dot{\boldsymbol{\nu}}$ in the bistable case are shown in Fig. 2F. An increase of the drive on the one hand increases the firing rate of the LA fixed point (inset) but on the other hand reduces its basin of attraction, indicated by the colored bars in the top left corner. For illustrative purposes, we extend the problem to two dimensions by splitting the excitatory population into two subpopulations of equal size, mimicking a loop between excitatory populations in the model of macaque visual cortex. The corresponding (symmetric) two-dimensional phase space is shown in Fig. 2D. The basin of attraction for the LA fixed point, limited by the separatrix (Strogatz, 1994), is reduced for increased external drive. Since we have a bistable system, there must be at least one unstable fixed point on the separatrix at the intersection of the nullclines, i.e., the subspace for which the velocity $\dot{\nu}_i$ in direction i vanishes. We use the unstable fixed point to control the basin of attraction. To this end, we study the behavior of the fixed points with respect to an infinitesimal change $\delta \mathbf{a} = \mathbf{a}' - \mathbf{a}$ in the chosen model parameter. Let $\boldsymbol{\nu}^*(\mathbf{a})$ and $\boldsymbol{\nu}^*(\mathbf{a}')$ be the corresponding locations of the fixed point and $\delta \boldsymbol{\nu}^* = \boldsymbol{\nu}^*(\mathbf{a}') - \boldsymbol{\nu}^*(\mathbf{a})$ their separation. We can then expand $\boldsymbol{\nu}^*(\mathbf{a}')$ into a Taylor series up to first order

in $\delta \mathbf{a}$ and obtain

$$\begin{aligned}\boldsymbol{\nu}^*(\mathbf{a}') &= \boldsymbol{\nu}^*(\mathbf{a}) + \boldsymbol{\Delta}_\mathbf{a} \delta \mathbf{a} \\ \Leftrightarrow \delta \boldsymbol{\nu}^* &= \boldsymbol{\Delta}_\mathbf{a} \delta \mathbf{a},\end{aligned}\tag{6}$$

with

$$\begin{aligned}\Delta_{\mathbf{a},ij} &= \frac{d\nu_i(\mu_i, \sigma_i)}{da_j} \\ &= \frac{d\Phi_i(\mu_i, \sigma_i)}{da_j} \\ &= \underbrace{\frac{\partial \Phi_i}{\partial \mu_i} \frac{d\mu_i}{da_j}}_{S_i} + \underbrace{\frac{\partial \Phi_i}{\partial \sigma_i} \frac{1}{2\sigma_i} \frac{d\sigma_i^2}{da_j}}_{T_i},\end{aligned}\tag{7}$$

where we notice that S_i and T_i only depend on the target population i . We accordingly define two diagonal matrices \mathbf{S} and \mathbf{T} with $S_{ii} = S_i$ and $T_{ii} = T_i$. The derivatives with respect to a_j have the compact expressions

$$\begin{aligned}\frac{d\mu_i}{da_j} &= \frac{\partial \mu_i}{\partial a_j} + \sum_n \frac{\partial \mu_i}{\partial \nu_n} \frac{d\nu_n}{da_j} \\ &= (\mathbf{D}_\mathbf{a}\boldsymbol{\mu})_{ij} + \tau_m \sum_n \underbrace{(K_{in} J_{in})}_{=W_{in}} \Delta_{\mathbf{a},nj},\end{aligned}$$

with the Jacobian $(\mathbf{D}_\mathbf{a}\mathbf{f})_{ij} := \frac{\partial f_i}{\partial a_j}$ of some vector-valued function \mathbf{f} and

$$\frac{d\sigma_i^2}{da_j} = (\mathbf{D}_\mathbf{a}\boldsymbol{\sigma}^2)_{ij} + \tau_m \sum_n \underbrace{(K_{in} J_{in}^2)}_{=W_{2,in}} \Delta_{\mathbf{a},nj},$$

where we use the Hadamard product again to define the matrix $\mathbf{W}_2 := \mathbf{K} \circledast \mathbf{J} \circledast \mathbf{J}$. Inserting the total derivatives into (7), we derive the final expression for $\boldsymbol{\Delta}_\mathbf{a}$, reading

$$\begin{aligned}\boldsymbol{\Delta}_\mathbf{a} &= \mathbf{S} [\mathbf{D}_\mathbf{a}\boldsymbol{\mu} + \tau_m \mathbf{W} \boldsymbol{\Delta}_\mathbf{a}] + \mathbf{T} [\mathbf{D}_\mathbf{a}\boldsymbol{\sigma}^2 + \tau_m \mathbf{W}_2 \boldsymbol{\Delta}_\mathbf{a}] \\ \Leftrightarrow \boldsymbol{\Delta}_\mathbf{a} &= \left[\mathbb{1} - \underbrace{\tau_m (\mathbf{S}\mathbf{W} + \mathbf{T}\mathbf{W}_2)}_{=: \mathbf{M}} \right]^{-1} \underbrace{[\mathbf{S}\mathbf{D}_\mathbf{a}\boldsymbol{\mu} + \mathbf{T}\mathbf{D}_\mathbf{a}\boldsymbol{\sigma}^2]}_{=: \bar{\boldsymbol{\Delta}}_\mathbf{a}},\end{aligned}\tag{8}$$

where we use $\mathbb{1}$ for the identity matrix and define the effective connectivity matrix \mathbf{M} and $\bar{\boldsymbol{\Delta}}_\mathbf{a}$. The latter is an $N \times P$ dimensional matrix, where P is the dimension of \mathbf{a} (for example, $P = N^2$ for $\mathbf{a} = \mathbf{k}$). With the aid of (8), evaluating (6) at the unstable fixed point predicts the shift of the separatrix (Fig. 2D) to linear order. We now consider an additional parameter \mathbf{b} which is modified to counteract the shift of the unstable fixed point caused by the change in parameter \mathbf{a} , i.e.,

$$\begin{aligned}\boldsymbol{\Delta}_\mathbf{a} \delta \mathbf{a} &\stackrel{!}{=} -\bar{\boldsymbol{\Delta}}_\mathbf{b} \delta \mathbf{b} \\ \Leftrightarrow \bar{\boldsymbol{\Delta}}_\mathbf{a} \delta \mathbf{a} &= -\bar{\boldsymbol{\Delta}}_\mathbf{b} \delta \mathbf{b},\end{aligned}\tag{9}$$

where we used in the last line that the inverse of $\mathbb{1} - \mathbf{M}$ appears on both sides of the equation and hence drops out. Note that \mathbf{a}, \mathbf{b} represent any combination of model parameters, for example external input, indegrees, synaptic weights, etc. For a particular choice of (\mathbf{a}, \mathbf{b}) we solve (9) for $\delta \mathbf{b}$. For the illustrative example shown in Fig. 2, where $a = \nu_{\text{ext}}$ and $b = K$, (9) simplifies to

$$\delta K = \frac{\bar{\Delta}_{\nu_{\text{ext}}} \delta \nu_{\text{ext}}}{\bar{\Delta}_K} = \frac{K_{\text{ext}} \delta \nu_{\text{ext}}}{\nu},$$

since the derivatives S and T appearing in the respective $\bar{\Delta}$'s cancel each other. The resulting velocity of the system $\Phi(a', b')$ (Φ defines the system (5)) is shown in Fig. 2F. The firing rate in the LA fixed point is still increased as desired (inset), and the unstable fixed point coincides with that obtained in the original system $\Phi(a, b)$. This pattern of fixed points is also indicated by the zero vectors of the velocity field $\dot{\boldsymbol{\nu}}$ (Fig. 2D). The separatrix follows the unstable fixed point, and the basin of attraction in the system $\Phi(a', b')$ is restored to that in the original system $\Phi(a, b)$. Fig. 2G shows the behavior of the LA fixed

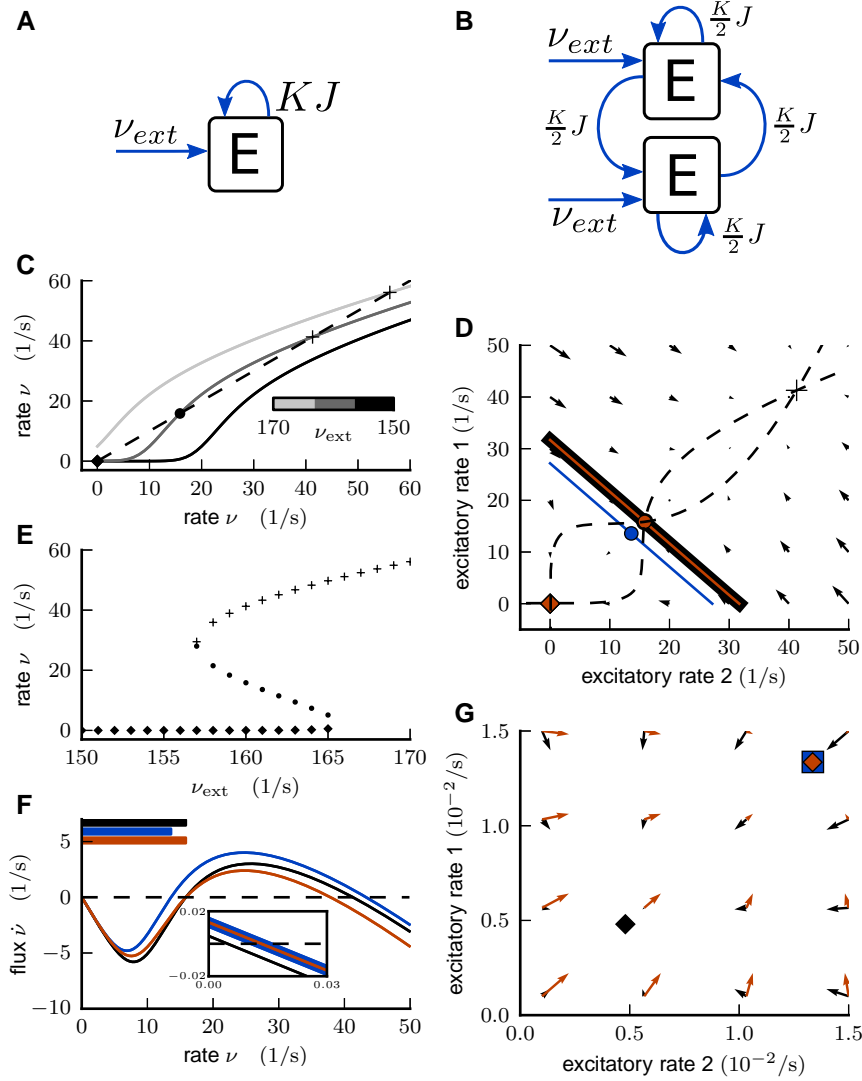


Figure 2: **Activity flow in an illustrative network example.** **Left column:** Global stability analysis in the single-population network. **A** Illustration of network architecture. **C** Input-output relationship $\Phi(\nu, \nu_{\text{ext}})$ for different rates of the external Poisson drive $\nu_{\text{ext}} = [150, 160, 170] \frac{1}{\text{s}}$ from black to light gray. Intersections with the identity line (dashed) mark fixed points of the system, which are shown in **E** as a function of ν_{ext} . **F** Flux $\dot{\nu}$ in the bistable case for $\Phi(\nu_{\text{ext}} = 160 \frac{1}{\text{s}}, K)$ (black) and $\Phi(\nu'_{\text{ext}} = 161 \frac{1}{\text{s}}, K)$ (blue) and modified system $\Phi(\nu'_{\text{ext}} = 161 \frac{1}{\text{s}}, K')$ (red). Intersections with zero (dashed line) mark fixed points. The inset shows an enlargement close to the LA fixed point. Horizontal bars at top of figure denote the size of the basin of attraction for each of the three settings. **Right column:** Global stability analysis in the network of two mutually coupled excitatory populations. **B** Illustration of network architecture. **D** Flow field and nullclines (dashed curves) for $\Phi(\nu_{\text{ext}} = 160 \frac{1}{\text{s}}, K)$ and separatrices (solid lines), LA fixed point (rectangle), HA fixed point (cross) and unstable fixed points (circles) for $\Phi(\nu_{\text{ext}} = 160 \frac{1}{\text{s}}, K)$ (black), $\Phi(\nu_{\text{ext}} = 161 \frac{1}{\text{s}}, K)$ (blue), $\Phi(\nu_{\text{ext}} = 161 \frac{1}{\text{s}}, K')$ (red). The red separatrix and the red unstable fixed point coincide with the black ones. **G** Enlargement of D close to the LA fixed points.

point in more detail. The modification of the parameter b does not change the location of the LA fixed point noticeably. In conclusion, the method allows us to increase the firing rates in the LA fixed point without modifying its basin of attraction.

To determine critical connections in a more complex model, we choose $\mathbf{b} = \mathbf{k}$ and solve (9) with a decomposition into eigenmodes. We can write the right-hand side as

$$-(\bar{\Delta}_{\mathbf{k}}\delta\mathbf{k})_i = -\sum_j \tau_m (S_i J_{ij} + T_i J_{ij}^2) \nu_j \delta K_{ij}. \quad (10)$$

The equation holds because μ_i, σ_i are only affected by connections to population i , and therefore their derivatives $\partial\mu_i/\partial k_l, \partial\sigma_i/\partial k_l$ and hence $\bar{\Delta}_{k,il}$, vanish for $l \notin [(i-1)N+1, iN]$. We now make the ansatz

$$\delta K_{ij} = \sum_l \frac{\epsilon_l}{\tau_m} \frac{(\mathbf{u}^l \mathbf{v}^{lT})_{ij}}{(\mathbf{S}\mathbf{J} + \mathbf{T}(\mathbf{J} \circledast \mathbf{J}))_{ij}}, \quad (11)$$

which decomposes the changes $\delta\mathbf{K}$ into eigenmodes of the effective connectivity. The \mathbf{u}^l and \mathbf{v}^l are the l -th right and left eigenvectors of \mathbf{M} (defined in (8)), fulfilling the bi-orthogonality $\mathbf{v}^{lT}\mathbf{u}^n = \delta_{ln}$ and the completeness relation $\sum_l \mathbf{u}^l \mathbf{v}^{lT} = \mathbf{1}$. Inserting (10) with (11) into (9) yields

$$\bar{\Delta}_{\mathbf{a}}\delta\mathbf{a} = -\sum_l \epsilon_l \mathbf{u}^l \mathbf{v}^{lT} \boldsymbol{\nu}. \quad (12)$$

We can solve for ϵ_l by multiplying from the left with \mathbf{v}^{nT}

$$\begin{aligned} \underbrace{\mathbf{v}^{nT} \bar{\Delta}_{\mathbf{a}} \delta \mathbf{a}}_{=: \hat{a}^n} &= -\sum_l \epsilon_l \underbrace{\mathbf{v}^{nT} \mathbf{u}^l}_{\delta_{nl}} \underbrace{\mathbf{v}^{lT} \boldsymbol{\nu}}_{=: \hat{\nu}^l} \\ \epsilon_n &= -\frac{\hat{a}^n}{\hat{\nu}^n}. \end{aligned}$$

Our goal is to find a set of connections which dominate the size of the basin of attraction of the LA fixed point. Inserting (12) into (6) leads to

$$\begin{aligned} \delta \boldsymbol{\nu}^* &= \sum_l (\mathbf{1} - \mathbf{M})^{-1} \epsilon_l \mathbf{u}^l \mathbf{v}^{lT} \boldsymbol{\nu} \\ &= \sum_l \frac{\epsilon_l}{1 - \lambda_l} \mathbf{u}^l \hat{\nu}^l \\ &= \sum_l \frac{-\hat{a}^l}{1 - \lambda_l} \mathbf{u}^l, \end{aligned}$$

where λ_l are the eigenvalues of \mathbf{M} , which are either real or complex conjugate pairs since $\mathbf{M} \in \mathbb{R}^{N \times N}$. To determine the influence of each eigenmode on the shift of the fixed point, we project the eigenvectors \mathbf{u}^l onto the fixed-point shift $\delta \boldsymbol{\nu}^*$ by multiplying each side with $\delta \boldsymbol{\nu}^* \delta \boldsymbol{\nu}^{*T}$ and solve again for $\delta \boldsymbol{\nu}^*$ to obtain

$$\delta \boldsymbol{\nu}^* = \sum_l \frac{-\hat{a}^l}{1 - \lambda_l} \underbrace{\frac{\delta \boldsymbol{\nu}^{*T} \mathbf{u}^l}{\delta \boldsymbol{\nu}^{*T} \delta \boldsymbol{\nu}^*}}_{=: \tilde{\eta}_l} \delta \boldsymbol{\nu}^*, \quad (13)$$

where we define the (possibly complex-valued) coefficients $\tilde{\eta}_l$. We aim at a decomposition of $\delta \boldsymbol{\nu}^*$ into real components. If $\text{Im}(\lambda_l) = 0$, $\tilde{\eta}_l$ is real, so we can work directly with $\eta_l := \tilde{\eta}_l$. Complex eigenvalues $\text{Im}(\lambda_l) \neq 0$ and corresponding eigenvectors come in conjugate pairs, so in this case we combine the corresponding coefficients $\eta_l := \tilde{\eta}_l + \tilde{\eta}_l^*$, to have all contributions $\eta_l \in \mathbb{R}$ and $\sum_l \eta_l = 1$ by construction (13). Each η_l quantifies how much of the total fixed-point shift can be attributed to the l -th eigenmode, which allows the identification of the most effective eigendirection (cf. Results). In the next section, we apply the ansatz (11) to a multi-area, multi-layer model of macaque visual cortex.

The spiking simulations of the network model are carried out with the NEST simulator (Gewaltig & Diesmann, 2007) on the JUQUEEN supercomputer (Stephan & Docter, 2015). All simulations can be reproduced with NEST 2.6.0, while the results presented in this study were performed with further optimizations for the supercomputer which will enter one of the next releases. All simulations use a time step of 0.1 ms and exact integration for the sub-threshold dynamics of the leaky integrate-and-fire neuron model (reviewed in Plesser & Diesmann, 2009).

Results

We investigate a multi-scale network of cortical areas to understand the structural features essential for a realistic state of baseline activity. The model extends and adapts the microcircuit model of Potjans & Diesmann (2014), which covers 1 mm² surface area of early sensory cortex, to all vision-related areas of macaque cortex (Fig. 3). Based on the microcircuit model, an area is composed of 4 layers (2/3, 4, 5, and 6) each having an excitatory (E) and an inhibitory (I) neural population (Fig. 3A), except parahippocampal area TH which consists of only 3 layers (2/3, 5, and 6). From anatomical studies, it is known that cortical areas in the macaque monkey are heterogeneous in their laminar structure and can be roughly categorized into 8 different architectural types based on cell densities and laminar thicknesses. This distinction was originally developed for prefrontal areas (Barbas & Rempel-Clower, 1997), and then extended to the entire cortex (C. Hilgetag and H. Barbas, personal communication). The visual cortex, and thus the model, comprises areas of categories 2,4,5,6,7 and 8. Precise layer-specific neuron densities are available for a number of areas, while for other areas, the neuron density is estimated based on their architectural type (see Schmidt et al. (2014) for details).

The inter-areal connectivity is based on binary data from the CoCoMac database (Stephan et al., 2001; Bakker et al., 2012; Felleman & Van Essen, 1991; Rockland & Pandya, 1979; Barnes & Pandya, 1992) indicating the existence of connections, and quantitative data from Markov et al. (2014a). The latter are retrograde tracing data where connection strengths are quantified by the fraction of labeled neurons (FLN) in each source area. The parcellation into different areas of our model follows the FV91 scheme proposed by Felleman & Van Essen (1991). The original analysis of the experimental data was performed in a different parcellation scheme, the M132 atlas of Markov et al. (2014a). Both parcellations have been registered to the F99 space (Van Essen, 2002), a standard macaque cortical surface included with the software tool Caret (Van Essen et al., 2001). This enables mapping between the two parcellations M132 and FV91.

On the target side, we use the exact coordinates of the injections to identify the equivalent area in the FV91 parcellation. To map the data on the source side from the M132 atlas to the FV91 parcellation, we count the number of overlapping triangles on the F99 surface between any given pair of regions and distribute data proportionally to the amount of overlap using tools available at the CoCoMac site (http://cocomac.g-node.org/services/f99_region_overlap.php). In the model, this FLN is mapped to the indegree K_{AB} the target area A receives from source area B divided by its total indegree, i.e., $FLN_{AB} = K_{AB} / \sum_{B'} K_{AB'}$. Here, K_{AB} is defined as the total number of synapses between A and B divided by the total number of neurons in A . On the source side, laminar connection patterns are based on CoCoMac (Felleman & Van Essen, 1991; Barnes & Pandya, 1992; Suzuki & Amaral, 1994; Morel & Bullier, 1990; Perkel et al., 1986; Seltzer & Pandya, 1994) and on fractions of labeled neurons in the supragranular layers (SLN) (Markov et al., 2014b). Gaps in these data are bridged exploiting a sigmoidal relation between SLN values and the logarithmized ratio of overall cell densities of the two areas. We map the SLN to the ratio between the number of synapses originating in layer 2/3 and the total number of synapses between the two areas, assuming that only excitatory populations send inter-area connections, i.e., $SLN_{AB} = \sum_i K_{AB}^{i,2/3E} N_A^i / \sum_{i,j} K_{AB}^{ij} N_A^i$, where the indices i and j go over the different populations within area A and B , respectively. On the target side, the CoCoMac database provides data from anterograde tracing studies (Felleman & Van Essen, 1991; Rockland & Pandya, 1979; Jones et al., 1978; Seltzer & Pandya, 1991). A detailed description of the data integration is given in Schmidt et al. (2014).

Simulations of the model (Fig. 3C) reveal that, though realistic levels of activity can be achieved for populations in layers 2/3 and 4, populations 5E and 6E of the majority of areas show vanishingly low activity in contrast to empirical data (Swadlow, 1988; de Kock & Sakmann, 2009). Missing inputs in the model, i.e., from subcortical and non-visual cortical areas, are replaced by Poissonian spike trains, whose rate ν_{ext} is a free, global parameter. In the original model all populations of a particular area receive the same indegree of external inputs K_{ext} . The only exception to this rule is area TH where the absence of the granular layer 4 is compensated by an increase of the external input to populations 23E and 5E by 20%. To elevate the firing rates in the excitatory populations in layers 5 and 6, we enhance the external Poisson drive, parametrized by the $K_{5E,\text{ext}}$ incoming connections per target neuron (indegree), of the 5E population by increasing $r = K_{5E,\text{ext}}/K_{\text{ext}}$. The simultaneous increase in the drive of 6E needs to be stronger, since the firing rates in population 6E of the original model (Fig. 3C) are even lower than the rates of 5E (averaged across areas: 0.09 spikes/s for 5E compared to $2 \cdot 10^{-5}$ spikes/s for 6E). We thus scale up $K_{6E,\text{ext}}$ linearly with r such that $r = 1.15$ results in $K_{6E,\text{ext}}/K_{\text{ext}} = 1.5$. However, already a perturbation in the range of a few percent leads to a state with unrealistically high rates (Fig. 3D), caused by the reduced basin of attraction of the low activity state similar to Fig. 2D. Our specific aim now is to improve the working point of the model such that all populations exhibit spiking activity ≥ 0.1 spikes/s while preventing the model from entering a state of unrealistically high rates of ≥ 30 spikes/s (Swadlow,

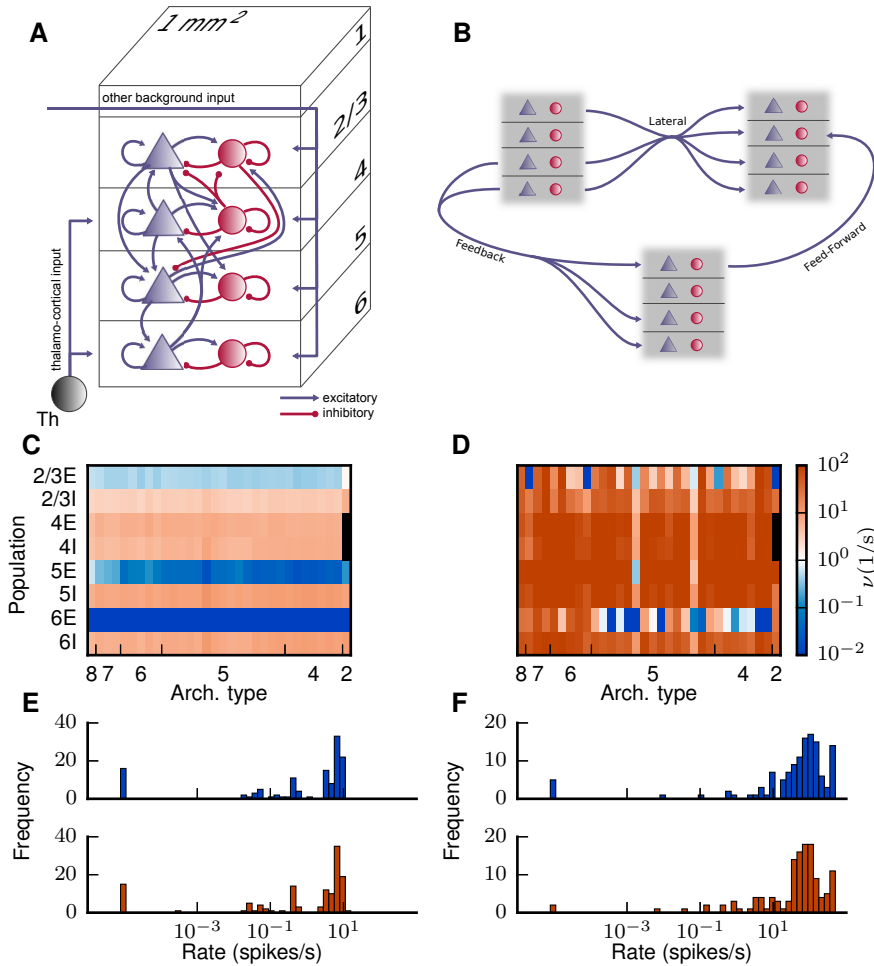


Figure 3: **Bistability of the model.** **A** Sketch of the microcircuit model serving as a prototype for the areas of the multi-area model (adapted from Potjans & Diesmann (2014)). **B** Sketch of the most common laminar patterns of cortico-cortical connectivity of the multi-area model. **C** Population-averaged firing rates encoded in color for a spiking network simulation of the multi-area model with low external drive ($r = 1.0$). **D** As **C** but for increased external drive ($r = 1.1$). The color bar refers to both panels. Areas are ordered according to their architectural type along the horizontal axis from V1 (type 8) to TH (type 2) and populations are stacked along the vertical axis. The two missing populations 4E and 4I of area TH are marked in black. **E** Histogram of population-averaged firing rates shown in **C** for excitatory (red) and inhibitory (blue) populations. **F** as **E** corresponding to state shown in **D**.

1988; de Kock & Sakmann, 2009). The employed technique exposes the mechanism giving rise to the observed instability and identifies the circuitry responsible for this dynamical feature.

The spiking network simulation settles in the LA state for $r = 1$ (Fig. 3C). Under these parameters the solution of the corresponding mean-field theory Φ (5) converges to the LA state only for initial conditions close to the inactive state $\nu(0) = (0, \dots, 0)^T$. Therefore, in the following we choose the inactive state as the initial condition. Fig. 4B shows the integration of (5) over the pseudo-time s for different increased levels of the external drive to populations 5E and 6E (parametrized by r). For low values of r , the integration converges to the LA fixed point, which is shown in Fig. 4D and is in agreement with the activity emerging in the simulation (Fig. 3C). For increased values of r , the system settles in the HA fixed point (Fig. 3E), again in agreement with the simulation. The population-specific firing rates in the HA state found in the mean-field predictions (Fig. 4E) are close to those in the simulation (Fig. 3D), but minor deviations occur due to the violation of the assumptions made in the diffusion approximation. In particular, at these pathologically high rates, the neurons fire regularly and close to the reciprocal of their refractory period, while in the mean-field theory we assume Poisson spike statistics. Still, the mean-field theory is able to quantitatively predict the bistability found in the simulation. Since the theory yields reliable predictions in both stable fixed points, we assume that also the location of the unstable fixed point in between these two extremes is accurately predicted by the theory.

To stabilize the LA fixed point for increased values of the external drive r , we apply the procedure derived in Theory and Methods. For this we need to find the unstable fixed point of the system. This is

nontrivial since the high-dimensional system of equations (2) is not directly solvable for the fixed-point firing rates, and the numerical integration of (5) for finding equilibria by construction only converges to stable fixed points. If the unstable fixed point has only one repelling direction (Fig. 6A), it constitutes a stable attractor on the $N - 1$ dimensional separatrix. The separatrix is a stable manifold (Strogatz, 1994), and therefore a trajectory originating in its vicinity but not near an unstable fixed point initially stays in the neighborhood. If the initial condition just outside the separatrix is close to the basin of attraction of a particular unstable fixed point, the trajectory initially approaches the latter. Close to the fixed point the velocity is small. Ultimately trajectories diverge from the separatrix in the fixed point's unstable direction, illustrated in Fig. 4A. In conclusion, we expect a local minimum in the velocity along the trajectories close to the unstable fixed point. To estimate the unstable fixed point in this manner, we need to find initial conditions which are close to the separatrix. Naively, we would just fix the value of r and vary the initial condition. However, due to the high dimensionality of our system, this is not feasible in practice, and we vary r for a fixed initial condition instead (cf. Fig. 4B), which is expected to yield the same qualitative result. Which of the unstable fixed points are found by this procedure may depend on the initial condition. As discussed, we use the silent state as the initial condition because it yields the LA state as in the simulation. Given this initial condition, the procedure by construction first yields the unstable fixed point that is approached when r is increased from its baseline value. In Fig. 4B we show the firing rate averaged across populations for two trajectories starting close to the separatrix, whereby the first one converges to the LA fixed point and the second one to the HA state. The trajectories diverge near the unstable fixed point and thus we define the last local minimum of the Euclidean norm of the velocity vector as the critical time s_c at which we assume the system to be close to the unstable fixed point (Fig. 4C). We find five relevant and distinct unstable fixed points, of which two are shown in Fig. 5.

To counteract the shift of the separatrix caused by the increase of r , we follow the procedure described in Theory and Methods. We subject the modifications of connectivity following from the application of the method to the following constraints. In line with the anatomical literature, we do not allow for changes of the connectivity that would lead to cortico-cortical connections originating in the granular layer 4, and we also disallow inhibitory cortico-cortical connections, as the vast majority of long-range connections are known to be excitatory (Salin & Bullier, 1995; Tomioka & Rockland, 2007). In addition, we naturally restrict indegrees to positive values. We find that five iterations (numbered by index j) corresponding to the five distinct unstable fixed points suffice to preserve the basin of attraction of the LA state with respect to an increase of the external drive up to $r = 1.19$. In the following we concentrate on the iterations 1 and 3, where the first one is also representative for the iterations 2,4 and 5, which are qualitatively alike. In each iteration j there is exactly one unstable eigendirection with an eigenvalue $\text{Re}(\lambda_c^{(j)}) > 1$ (Fig. 6A). The associated critical eigenvector is approximately anti-parallel to the shift of the fixed point, $\delta\nu^*$ (inset of Fig. 6B), and of similar length. The critical eigendirection (red dot in Fig. 6B) thus constitutes the most effective modification, giving the largest contribution to the desired shift but requiring only a small change of 0.5%.

The associated eigenvector $u_c^{(1)}$ has large entries in the 5E populations of two areas (Fig. 6C), while $u_c^{(3)}$ points into the direction of populations 4E and 5E of areas FEF and 46 (Fig. 6D). The high rates of these populations at the unstable fixed points (cf. Fig. 5A,B with Fig. 6C,D) reflect that the instability is caused by increased rates in excitatory populations. Considering the other iterations (not shown) as well, these instabilities occur particularly in population 5E. Fig. 7A shows how each iteration shifts the transition to the HA state (the value of r for which the separatrix crosses the initial condition) to higher values of r and increases the maximal rates of populations 5E and 6E in the LA state. After all five iterations, the summed indegrees of the system are changed by 5.4%. In the first iteration, the changes are spread across areas (Fig. 7B). The third iteration mainly affects connections within and between areas 46 and FEF (Fig. 7C). In particular, the excitatory loops between the two areas are reduced in strength, especially those involving layer 5 (Fig. 7D). In the third iteration, we thus identify two areas forming a critical loop. In conclusion, the method is able to identify critical structures in the model both on the level of areas and on the level of layers and populations, and leads to a small but specific change of the structure of the model.

In the following we analyze the modifications of the connectivity with respect to the internal and inter-area connections in detail. The intrinsic circuits of the areas are modified in different directions, as shown for two exemplary areas V4 and CITv in Fig. 8A. Despite this heterogeneity, significant changes affect mostly excitatory-excitatory connections (Fig. 8A) with connections to population 5E experiencing the most significant changes (Fig. 7B,D). In fact, the anatomical data (Binzegger et al., 2004) underlying the microcircuit model (Potjans & Diesmann, 2014) contain only two reconstructed excitatory cells from layer 5, but considerably more for other cell types, indicating a higher uncertainty for layer 5 connections. Fig. 8B shows the correlation between intrinsic connectivity changes for all pairs of areas, with areas ordered according to a hierarchical clustering using a farthest point algorithm (Voorhees, 1986) on the

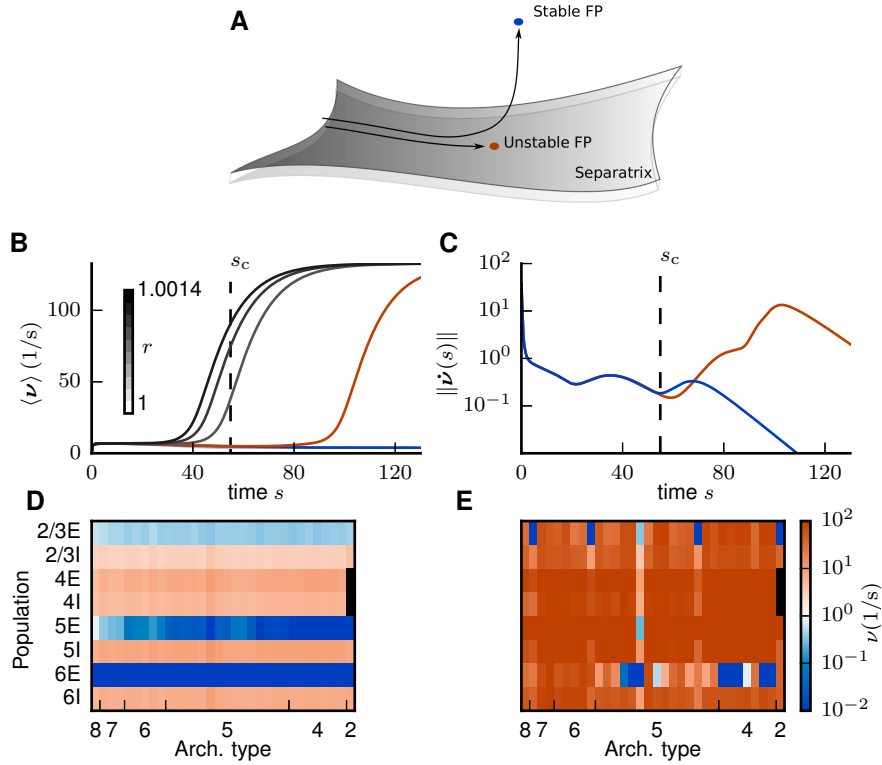


Figure 4: **Application of the mean-field theory to the multi-area model of visual cortex.** **A** Trajectories starting inside the separatrix converge to an unstable fixed point. Trajectories starting close to the separatrix are initially attracted by the unstable fixed point but then repelled in the fixed point's unstable direction and finally converge to a stable fixed point. **B** Firing rate averaged across populations over time. Integration of (5) leads to convergence to either the low-activity (LA) or the high-activity (HA) attractor for different choices of the external input factor r . We show eight curves with r varying from 1.0 to 1.0014 in steps of 0.0002 and an additional curve for $r = 1.0007975$. The curves for the largest factor ($r = 1.0007975$) that still leads to the LA state and for the smallest factor ($r = 1.0008$) that leads to the HA state are marked in blue and red, respectively. The four curves with $r \leq 1.0006$ coincide with the blue curve. **C** Euclidean norm of the velocity vector in the integration of (5) for the different choices of r . The vertical dashed line indicates the time s_c of the last local minimum in the blue curve. **D** Stationary firing rate in the different areas and layers of the model in a low-activity state for $r = 1.0$ as predicted by the mean-field theory (same display as in Fig. 3). **E** As **D**, but showing the high-activity state for $r = 1.1$.

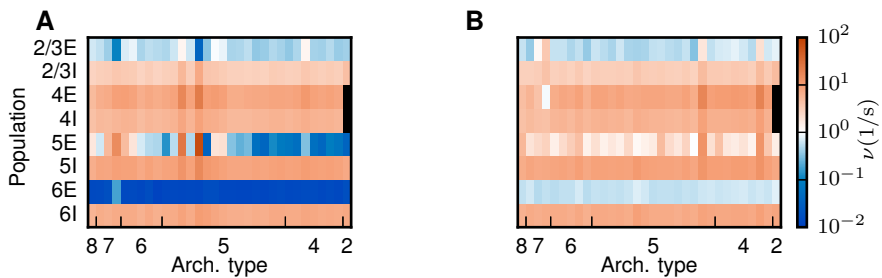


Figure 5: **Unstable fixed points in subsequent iterations.** Population firing rates at the unstable fixed point as predicted by the mean-field theory encoded in color for iterations 1 (**A**) and 3 (**B**). Same display as in Fig. 3.

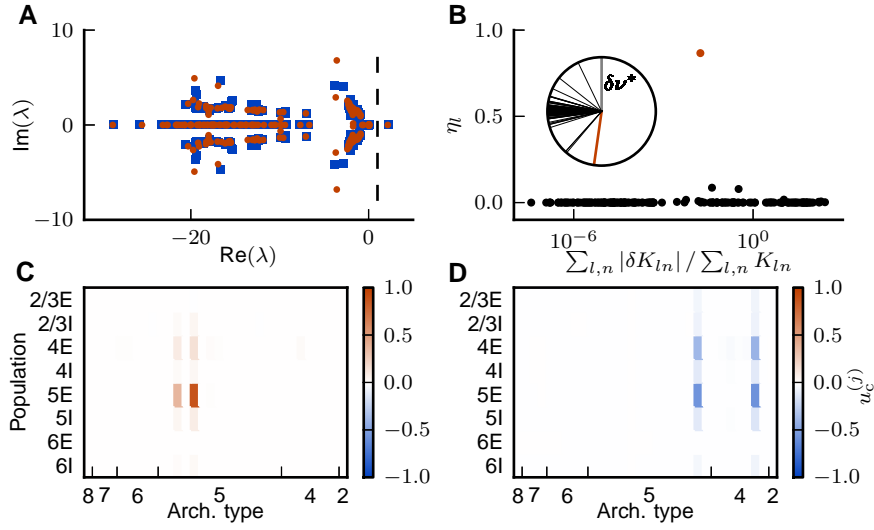


Figure 6: **Eigenspectrum analysis of network stability.** **A** Eigenvalue spectrum of the effective connectivity matrix M for the first (blue squares) and third (red dots) iteration. The dashed vertical line marks the edge of stability at a real part of 1. **B** Contribution η_l of an individual eigenprojection l to the shift of the unstable fixed point (13) versus the relative change in indegrees associated with l for the first iteration. The data point corresponding to $\lambda_c^{(1)}$ is marked in red. The inset shows the relative angles between $\delta\nu^*$ and the eigenvectors \mathbf{u}^l . The red line corresponds to the critical eigendirection. **C** Entries of the eigenvector $u_c^{(1)}$ associated with $\lambda_c^{(1)}$ in the populations of the model. **D** Same as **C** for the third iteration. The affected areas are 46 and FEF.

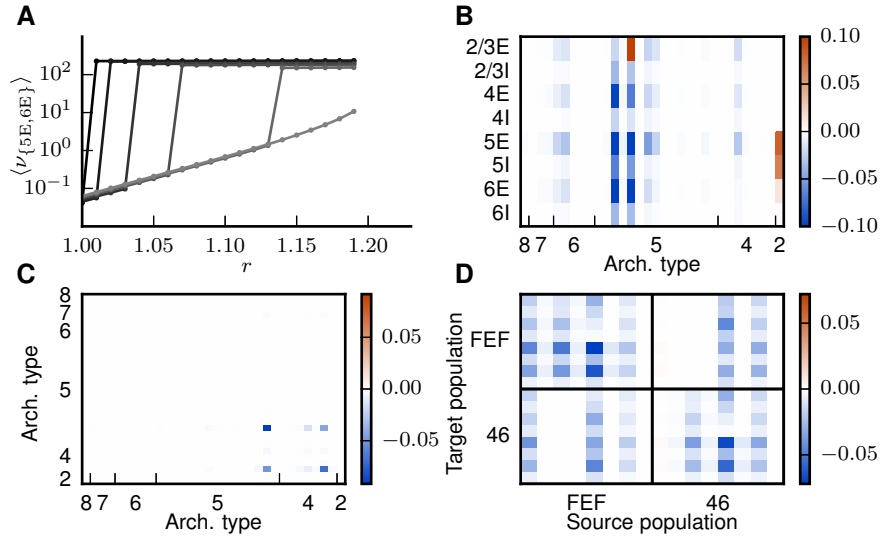


Figure 7: **Altered phase space and modified connections.** **A** Firing rates of populations 5E and 6E averaged across areas for different stages from the original model (black) to iteration 5 (light gray) as a function of r , as predicted by the mean-field theory. **B** Relative changes in population-specific indegrees summed over source populations, $\sum_n \delta K_{ln} / \sum_n K_{ln}$, for the first iteration. **C** Relative changes in the indegree $\delta K_{AB} / \sum_B K_{AB}$ between areas A, B in the third iteration. **D** Layer-specific relative changes $\delta K_{ln} / \sum_n K_{ln}$ in the connections within and between areas FEF and 46, for the third iteration. Populations are ordered from 2/3E (left) to 6I (right) on the horizontal axis and from 6I (bottom) to 2/3E (top) on the vertical axis as in panel **B**.

correlation matrix. We find 6 clusters each indicating a group of areas which undergo changes with similar patterns. The groups are displayed in different colors in the histogram in Fig. 8B. Areas with architectural type 4, 5 and 6 are distributed over several clusters. We can understand this as a differentiation of these types into further subtypes. The resulting changes of the intra-areal connectivity are very small (Fig. 8A), but still significant for network stability.

Connections between areas can be characterized by their FLN and SLN . The FLN reflects the overall strength of an inter-areal connection and is only weakly affected across connections (Fig. 8C), with a correlation between original and modified logarithms of FLN of $r_{\text{Pearson}} = 0.78$. Significant variations in the FLN occur mostly for very weak connections where the relative uncertainties in the experimental data are likely to be substantial. The two overlapping red dots in Fig. 8C represent the connections between areas 46 and FEF, which are modified in the third iteration (cf. Fig. 7C). The SLN determines the laminar pattern of the location of source neurons for cortico-cortical connections. Overall, data are available for 24% of the inter-areal connections in the parcellation of Felleman & Van Essen (1991), while the SLN for the rest are derived from the sigmoidal law. The majority of connections undergo small changes in their laminar source pattern (Fig. 8D) and connections with large modifications ($|\delta SLN| > 0.5$) are weak (average $\overline{FLN} = 5 \cdot 10^{-4}$ compared to $\overline{FLN} = 5 \cdot 10^{-3}$ in the model as a whole). Because weak connections are represented by low neuron counts, they have a relatively large uncertainty in their laminar patterns, justifying larger adjustments. Spearman’s rank correlation between the SLN of the original model that were directly taken from experiments and the logarithmized ratios of cell densities is $\rho = -0.71$ ($p = 10^{-20}$, p-value of a two-sided test for uncorrelated data). For the modified model, we take the SLN of all connections into account and obtain $\rho = -0.23$ ($p = 8 \cdot 10^{-8}$), indicating a reduced, but still significant, monotonic dependence between SLN and the logarithmized ratios of cell densities.

We quantify the variability of the cortico-cortical connections (Markov et al., 2014a) as the average inter-individual standard deviation of the logarithmic FLN , i.e., $\sigma = \left\langle \sqrt{\sum_i (\log FLN_i - \overline{\log FLN})^2 / N} \right\rangle$,

where i is the summation index over N repeat injections and $\langle \rangle$ is the average over connections. This variability equals 2.17 while the average modification of the logarithmic FLN is 1.02. The main experimental connection probabilities used to construct the intra-areal connectivity of the model have an average relative standard deviation of 30% across electrophysiological experiments (cf. Table 1 of Potjans & Diesmann, 2014) while the intra-areal connection probabilities of the model are modified by 9% on average. Scannell et al. (2000) report even greater variability in a review on cortico-cortical and thalamo-cortical connectivity. These considerations show that the changes applied to the connectivity are well within the uncertainties of the data. Overall, 35 out of 603 connections were removed from the network. In the CoCoMac database, 77% of these are indicated by only a single tracer injection, while the overall proportion of connections measured by a single injection is 59%.

Simulation of the full spiking network model with the modified connectivity matrix results in reasonable rates across populations and areas (Fig. 9). The average rates in populations 5E and 6E are increased compared to a simulation of the original model from 0.09 and $2 \cdot 10^{-5}$ spikes/s to 5.9 and 0.9 spikes/s, respectively. All populations exhibit firing rates within a reasonable range between 0.1 and 30 spikes/s (Fig. 9D), as opposed to the original state in which a considerable fraction of excitatory neurons was silent (Fig. 3E). In almost all populations, the theoretical prediction is in agreement with the rates obtained in the simulation (Fig. 9C). Deviations are observed for very low rates, where the activity is underestimated by the analytical theory. This discrepancy, arising from the employed approximations (Fourcaud & Brunel, 2002), is negligible for the network’s stability, due to the limited influence of nearly silent populations. The two obvious deviations apparent for higher firing rates occur in the excitatory population of layer 5 in areas V3 and TH. In the simulated data we observe a broad distribution of firing rates over neurons in V3 and bursty spiking in TH (data not shown). Both these effects are not included in the theory and presumably cause the observed discrepancies.

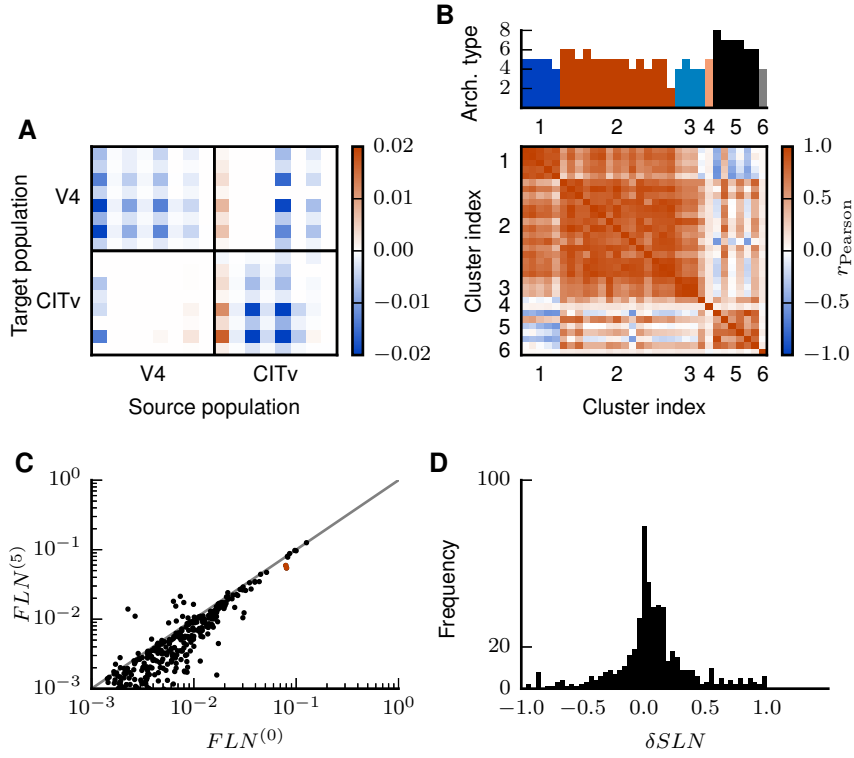


Figure 8: **Analysis of changes in connectivity.** **A** Changes in the indegrees within and between exemplary areas V4 and CITv relative to the total indegrees of the target populations, i.e., $\delta K_{ln} / \sum_n K_{ln}$. Populations ordered as in Fig. 7C. **B** Pearson correlation coefficient of the changes of the internal indegrees δK_{AA}^{ij} between all pairs of the 32 areas. Areas ordered according to hierarchical clustering using a farthest point algorithm (Voorhees, 1986). The heights of the bars on top of the matrix indicate the architectural types of the areas (types 1 and 3 do not appear in the model) with color representing the respective clusters. **C** FLN of the modified connectivity after 5 iterations versus the original FLN of the model. Only $FLN > 10^{-3}$ are shown for a better overview. The overlapping red dots represent the connections between areas 46 and FEF. Unity line shown in gray. **D** Histogram of the changes in SLN ($\delta SLN = SLN^{(5)} - SLN^{(0)}$).

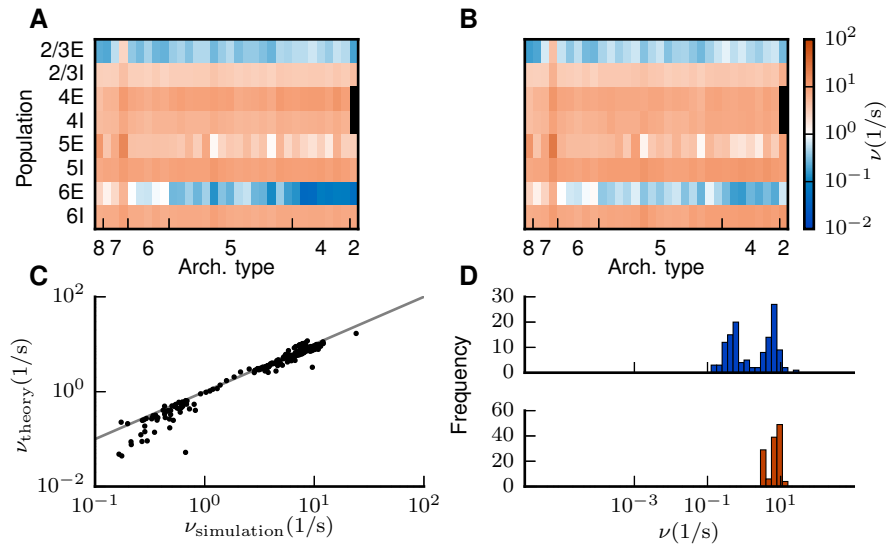


Figure 9: **Improved low-activity fixed point of the model.** Population-averaged firing rates for $r = 1.15$ encoded in color (**A**) predicted by the analytical theory and (**B**) obtained from the full simulation of the spiking network. Same display as in Fig. 3. **C** Analytical versus simulated firing rates (black dots) and identity line (gray). **D** Histogram of population-averaged simulated firing rates in excitatory (blue) and inhibitory (red) populations for the state shown in **B**.

Discussion

This study investigates the link between experimentally measured structural connectivity and neuronal activity in a multi-scale spiking neural network model of macaque visual cortex (Schmidt et al., 2014). We devise a theoretical method that allows us to systematically combine anatomical connectivity with physiological activity constraints. Already with the weak constraint of the activity neither vanishing nor being pathologically high, the method yields a set of specific but minimal structural modifications for increasing the excitation of the model to a realistic level. The procedure constrains the experimentally obtained connectivity maps to a realization that is compatible with physiological experiments. This establishes a path from the experimentally observed activity to specific hypotheses about the anatomy and demands for further experiments.

Connections are modified both within and between cortical areas, well within the known uncertainties of the underlying data. The areas of the model are based on the circuit of Potjans & Diesmann (2014), which models early sensory cortex. This circuit is adapted to the individual areas by taking into account neuronal densities and laminar thicknesses. The model definition renders areas with equal architectural type very similar in their internal connectivity. This is a drastic but inevitable simplification due to the lack of more detailed experimental data. The method softens this assumption, distinguishing the architectural types into further subtypes with small adaptations to their internal connectivity, which are significant for the global stability of the network. Thus, our approach enables purely anatomy-based area categorizations to be refined with dynamical information.

Connections between areas are changed in terms of both total strength and laminar patterns. Overall, the changes are small, but significant for specific connections. The loop formed by the two areas 46 and FEF is critical to the global stability of the network. Both areas have been investigated by Markov et al. (2014a), albeit in a different parcellation scheme than the Felleman & Van Essen (1991) scheme used in the present work. Our method suggests a weaker coupling of these two areas than found in the anatomical data set. Uncertainties partly due to the mapping between the parcellations leave room for this interpretation. Areas 46 and FEF belong to the prefrontal cortex and are multimodal, indicating that the influence of other parts of cortex could make them more stable, a factor not included in the visual cortex model. Both explanations can be tested either in an experimental study or with an extended model.

A few weak connections undergo large changes in their laminar patterns. With the present constraints, the method hereby weakens hierarchical relations in the model structure, indicating that preserving these relations requires additional dynamical constraints such as layer-specific coherence between areas (van Kerkoerle et al., 2014; Bastos et al., 2015). Conversely, it is possible to achieve satisfactory population rates with a less pronounced hierarchical structure in the model.

Our analysis reveals that layer 5 excitatory cells play a critical role for the dynamics of the model, in line with experimental studies on the ongoing dynamics in mammalian neocortex (Sanchez-Vives & McCormick, 2000; Beltramo et al., 2013). This critical role is often attributed to single-neuron properties, with a subset of layer 5 neurons displaying pacemaker activity (see, e.g., Le Bon-Jego & Yuste, 2007). We find that the network architecture itself already explains a strong impact of layer 5 on the phase space of the network.

The cortico-cortical connectivity of the model is compiled from the CoCoMac database (Stephan et al., 2001; Bakker et al., 2012), which collects data from hundreds of tracing studies, and the extensive dataset of Markov et al. (2014a). One could consider alternative methods for combining this information into one connectivity graph, for instance taking into account how consistently a given connection is reported across studies (Schmitt et al., 2014), and compare the different methods by analyzing the resulting network dynamics. The presented mean-field theory could then be used to estimate the firing rates of each network instance without performing time-consuming simulations. We choose the integrative approach that first accumulates all available experimental evidence into a single model and then modify the resulting connectivity with our analytical procedure. Our analysis shows that the method effectively sorts out uncertain connections.

The analytical theory uses the diffusion approximation to derive a self-consistent equation for the stationary population rates which is valid if indegrees are high while single synaptic events have minor impact. These requirements are fulfilled in the multi-area model and therefore the theoretical prediction agrees with the stationary activity of the simulation. Moreover, the theory predicts the bistability of the model, which is non-trivial, as it is derived under the assumption of near-Poisson statistics of the activity generally violated in the high-activity state. Nevertheless, since the activity in this state is mostly driven by strong mean inputs and the mean-field theory converges to the noiseless solution in the mean-driven limit, its predictions still provide a viable approximation. The firing rates in the unstable fixed points are predominantly low, while the exceptions with very high rates are again mean-dominated. Therefore, the locations of these attractors are presumably well predicted by the theory, and, in consequence, global

stability properties are accurately described. To preserve the global stability of the system while increasing the activity of the low-activity fixed point, we need to keep the position of the separatrix invariant, which we approximately achieve by preserving the location of the unstable fixed points on the separatrix. To this end, we use a linearization around these locations and an eigenmode decomposition in order to identify sets of connections to adjust, on both the area and the population level. In the multi-area model, this is justified because the system operates close to an instability so that only minor modifications are required. The method can be generalized to larger modifications by changing parameters iteratively in small steps.

In this study we restrict ourselves to leaky integrate-and-fire model neurons. This simplification is a key concept of the models we consider: individual cells are modeled in a simple manner to expose the impact of structural connectivity on the network dynamics. Moreover, the current-based leaky integrate-and-fire neuron can reproduce in-vivo like activity (Rauch et al., 2003; La Camera et al., 2004; Jolivet et al., 2006) and is analytically tractable, which enables the identification of mechanisms underlying specific network effects. More complex neuron models can be easily incorporated into the theory by replacing the gain function of each neuron population, be it by an analytical expression, if available, or by an interpolated function obtained from spiking single-neuron simulations. For example, one could use a conductance-based point-neuron model. These models feature a non-monotonic gain function, i.e., their gain is reduced if excitatory and inhibitory inputs are increased in a balanced manner (Kuhn et al., 2004). Generally, this renders a system more stable. However, the bistability considered in our work is caused by excitatory inputs. Since also conductance-based models show a monotonically increasing gain function in dependence of the excitatory conductance alone, we expect the bistability to occur also for such models.

Biological networks have various stabilization mechanisms not considered here, which render them less critical. For example, during growth, homeostatic mechanisms guide the system toward the right structure. Furthermore, short-term synaptic plasticity (reviewed in Morrison et al., 2008), homeostatic synaptic scaling (Turrigiano et al., 1998) and spike-frequency adaptation (e.g. summarized in Benda & Herz, 2003) may prevent the system from entering the high-activity state. However, introducing these self-organizing mechanisms increases model complexity, hindering a deep understanding of the relation between structure and activity. Therefore, we here take the approach of starting from a mean-field description on the level of neuronal populations, ignoring details of synaptic dynamics. Mild constraints on the activity guide us to a network structure within the anatomical range of parameters. This network yields globally stable activity, suggesting that the stabilization mechanisms mentioned are not a necessity to achieve this.

The observed inter-individual variability may reflect that mechanisms of self-organization and homeostasis find structurally different implementations of the same function. Thus, in studies across individuals we cannot expect that with progress in experimental technology the variability of parameters is narrowed down indefinitely. The combined ranges of parameters rather specify the space in which solutions can be found, and our method provides a way to find them.

In principle, the method applies to any model parameter. Here, we concentrated on indegrees, but it would be possible to modify, for example, the synaptic weights. Since experimental data on synaptic weights are sparse, this is another natural choice. Moreover, such an analysis may provide hints about suitable synaptic plasticity rules that dynamically stabilize the model.

Experimental data on stationary activity in cortex are sparse, and therefore we restrict ourselves to fundamental constraints and increase the drive to the model in an area-unspecific way to fulfill them. The resulting heterogeneity of the firing rates across areas is thus not imposed by the method, but rather arises from the connectivity that remains strongly informed by anatomical data. Alternatively, one could predefine a desirable state and investigate the set of parameter changes necessary to achieve it.

In the present work, the analytical combination of anatomy and activity data into a consistent model is restricted to stationary firing rates. In future studies, also higher-order statistical measures of activity can be used as constraints. Resting-state fMRI, for example, provides information on the functional connectivity between areas as a second-order measure. When combined with analytical predictions of functional connectivity, the method may shed light on the anatomical connection patterns underlying inter-area communication.

Acknowledgements

Use of the JUQUEEN supercomputer by VSR computation time grant JINB33. Partly supported by Helmholtz Portfolio Supercomputing and Modeling for the Human Brain (SMHB), the Helmholtz young investigator group VH-NG-1028, EU Grant 269921 (BrainScaleS), and EU Grant 604102 (Human Brain Project, HBP). All network simulations carried out with NEST (<http://www.nest-simulator.org>).

References

- Abramowitz, M., & Stegun, I. A. (1974). *Handbook of Mathematical Functions: with Formulas, Graphs, and Mathematical Tables*. New York: Dover Publications.
- Amit, D. J., & Brunel, N. (1997a). Dynamics of a recurrent network of spiking neurons before and following learning. *Network: Comput. Neural Syst.* 8, 373–404.
- Amit, D. J., & Brunel, N. (1997b). Model of global spontaneous activity and local structured activity during delay periods in the cerebral cortex. *Cereb. Cortex* 7, 237–252.
- Axer, M., Grassel, D., Kleiner, M., Dammers, J., Dickscheid, T., Reckfort, J., Hütz, T., Eiben, B., Pietrzyk, U., Zilles, K., et al. (2011). High-resolution fiber tract reconstruction in the human brain by means of three-dimensional polarized light imaging. *Frontiers in neuroinformatics* 5(34).
- Bakker, R., Thomas, W., & Diesmann, M. (2012). Cocomac 2.0 and the future of tract-tracing databases. *Front Neuroinform.* 6(30).
- Barbas, H., & Rempel-Clower, N. (1997). Cortical structure predicts the pattern of corticocortical connections. *Cerebral Cortex* 7(7), 635–646.
- Barnes, C. L., & Pandya, D. N. (1992). Efferent cortical connections of multimodal cortex of the superior temporal sulcus in the rhesus monkey. *Journal of Comparative Neurology* 318(2), 222–244.
- Barone, P., Batardiere, A., Knoblauch, K., & Kennedy, H. (2000). Laminar distribution of neurons in extrastriate areas projecting to visual areas v1 and v4 correlates with the hierarchical rank and indicates the operation of a distance rule. *J. Neurosci.* 20(9), 3263–3281.
- Bastos, A. M., Vezoli, J., Bosman, C. A., Schoffelen, J.-M., Oostenveld, R., Dowdall, J. R., De Weerd, P., Kennedy, H., & Fries, P. (2015). Visual areas exert feedforward and feedback influences through distinct frequency channels. *Neuron* 85(2), 390–401.
- Beltramo, R., D’Urso, G., Maschio, M. D., Farisello, P., Bovetti, S., Clovis, Y., Lassi, G., Tucci, V., Tonelli, D. D. P., & Fellin, T. (2013). Layer-specific excitatory circuits differentially control recurrent network dynamics in the neocortex. *Nature Neuroscience* 16(2), 227–234.
- Benda, J., & Herz, V. (2003). A universal model for spike-frequency adaptation. *Neural Comput.* 15, 2523–2546.
- Binzegger, T., Douglas, R. J., & Martin, K. A. C. (2004). A quantitative map of the circuit of cat primary visual cortex. *J. Neurosci.* 39(24), 8441–8453.
- Cabral, J., Kringelbach, M. L., & Deco, G. (2014). Exploring the network dynamics underlying brain activity during rest. *Prog Neurobiol* 114, 102–131.
- Cichocki, A., Zdunek, R., Phan, A. H., & Amari, S.-i. (2009). *Nonnegative matrix and tensor factorizations: applications to exploratory multi-way data analysis and blind source separation*. John Wiley & Sons.
- Cole, M. W., Bassett, D. S., Power, J. D., Braver, T. S., & Petersen, S. E. (2014). Intrinsic and task-evoked network architectures of the human brain. *Neuron* 83(1), 238–251.
- de Kock, C. P. J., & Sakmann, B. (2009). Spiking in primary somatosensory cortex during natural whisking in awake head-restrained rats is cell-type specific. *Proc. Natl. Acad. Sci. USA* 106(38), 16446–16450.
- Deco, G., & Jirsa, V. K. (2012). Ongoing cortical activity at rest: Criticality, multistability, and ghost attractors. *The Journal of Neuroscience* 32(10), 3366–3375.
- Felleman, D. J., & Van Essen, D. C. (1991). Distributed hierarchical processing in the primate cerebral cortex. *Cereb. Cortex* 1, 1–47.
- Fourcaud, N., & Brunel, N. (2002). Dynamics of the firing probability of noisy integrate-and-fire neurons. *Neural Comput.* 14, 2057–2110.
- Gewaltig, M.-O., & Diesmann, M. (2007). NEST (NEural Simulation Tool). *Scholarpedia* 2(4), 1430.

- Goulas, A., Bastiani, M., Bezgin, G., Uylings, H. B., Roebroeck, A., & Stiers, P. (2014). Comparative analysis of the macroscale structural connectivity in the macaque and human brain. *PLoS Comput Biol* 10(3), e1003529.
- Helias, M., Tetzlaff, T., & Diesmann, M. (2013). Echoes in correlated neural systems. *New J. Phys.* 15, 023002.
- Hu, Y., Trousdale, J., Josić, K., & Shea-Brown, E. (2013). Motif statistics and spike correlations in neuronal networks. *Journal of Statistical Mechanics: Theory and Experiment* 2013(03), P03012.
- Jolivet, R., Rauch, A., Lüscher, H.-R., & Gerstner, W. (2006). Predicting spike timing of neocortical pyramidal neurons by simple threshold models. *J. Comput. Neurosci.* 21(1), 35–49.
- Jones, E., Coulter, J., & Hendry, S. (1978). Intracortical connectivity of architectonic fields in the somatic sensory, motor and parietal cortex of monkeys. *Journal of Comparative Neurology* 181(2), 291–347.
- Kuhn, A., Aertsen, A., & Rotter, S. (2004). Neuronal integration of synaptic input in the fluctuation-driven regime. *J. Neurosci.* 24(10), 2345–2356.
- La Camera, G., Rauch, A., Luscher, H., Senn, W., & Fusi, S. (2004). Minimal models of adapted neuronal response to in vivo-like input currents. *Neural Comput.* 10(16), 2101–2124.
- Le Bon-Jego, M., & Yuste, R. (2007). Persistently active, pacemaker-like neurons in neocortex. *Frontiers in neuroscience* 1(1), 123.
- Magnus, J. R., & Neudecker, H. (1995). *Matrix differential calculus with applications in statistics and econometrics*. John Wiley & Sons.
- Markov, N. T., Ercsey-Ravasz, M., Van Essen, D. C., Knoblauch, K., Toroczkai, Z., & Kennedy, H. (2013). Cortical high-density counterstream architectures. *Science* 342(6158), 1238406.
- Markov, N. T., Ercsey-Ravasz, M. M., Ribeiro Gomes, A. R., Lamy, C., Magrou, L., Vezoli, J., Misery, P., Falchier, A., Quilodran, R., Gariel, M. A., Sallet, J., Gamanut, R., Huissoud, C., Clavagnier, S., Giroud, P., Sappey-Marinié, D., Barone, P., Dehay, C., Toroczkai, Z., Knoblauch, K., Van Essen, D. C., & Kennedy, H. (2014a). A weighted and directed interareal connectivity matrix for macaque cerebral cortex. *Cerebral Cortex* 24(1), 17–36.
- Markov, N. T., Vezoli, J., Chameau, P., Falchier, A., Quilodran, R., Huissoud, C., Lamy, C., Misery, P., Giroud, P., Ullman, S., Barone, P., Dehay, C., Knoblauch, K., & Kennedy, H. (2014b). Anatomy of hierarchy: Feedforward and feedback pathways in macaque visual cortex. *Journal of Comparative Neurology* 522(1), 225–259.
- Morel, A., & Bullier, J. (1990). Anatomical segregation of two cortical visual pathways in the macaque monkey. *Visual neuroscience* 4(06), 555–578.
- Morrison, A., Diesmann, M., & Gerstner, W. (2008). Phenomenological models of synaptic plasticity based on spike-timing. *Biol. Cybern.* 98, 459–478.
- Ostojic, S., Brunel, N., & Hakim, V. (2009). How connectivity, background activity, and synaptic properties shape the cross-correlation between spike trains. *J. Neurosci.* 29(33), 10234–10253.
- Perkel, D. J., Bullier, J., & Kennedy, H. (1986). Topography of the afferent connectivity of area 17 in the macaque monkey: A double-labelling study. *Journal of Comparative Neurology* 253(3), 374–402.
- Pernice, V., Staude, B., Cardanobile, S., & Rotter, S. (2011). How structure determines correlations in neuronal networks. *PLoS Comput. Biol.* 7(5), e1002059.
- Pernice, V., Staude, B., Cardanobile, S., & Rotter, S. (2012). Recurrent interactions in spiking networks with arbitrary topology. *Phys. Rev. E* 85(3), 031916.
- Plesser, H. E., & Diesmann, M. (2009). Simplicity and efficiency of integrate-and-fire neuron models. *Neural Comput.* 21, 353–359.
- Potjans, T. C., & Diesmann, M. (2014). The cell-type specific cortical microcircuit: Relating structure and activity in a full-scale spiking network model. *Cereb. Cortex* 24(3), 785–806. doi: 10.1093/cercor/bhs358.

- Rauch, A., La Camera, G., Lüscher, H., Senn, W., & Fusi, S. (2003). Neocortical pyramidal cells respond as integrate-and-fire neurons to in vivo like input currents. *J. Neurophysiol.* *90*, 1598–1612.
- Rockland, K. S., & Pandya, D. N. (1979). Laminar origins and terminations of cortical connections of the occipital lobe in the rhesus monkey. *Brain Res.* *179*, 3–20.
- Salin, P.-A., & Bullier, J. (1995). Corticocortical connections in the visual system: structure and function. *Physiological Reviews* *75*(1), 107–154.
- Sanchez-Vives, M. V., & McCormick, D. (2000). Cellular and network mechanisms of rhythmic recurrent activity in neocortex. *Nature Neuroscience* *3*, 1027–1034.
- Scannell, J. W., Grant, S., Payne, B. R., & Baddeley, R. (2000). On variability in the density of corticocortical and thalamocortical connections. *Philosophical Transactions of the Royal Society of London B: Biological Sciences* *355*(1393), 21–35.
- Schmidt, M., Schuecker, J., Diesmann, M., & Helias, M. (2015). Shaping phase space of neural networks via connectivity. In *Proceedings of the 11th Göttingen Meeting of the German Neuroscience Society*, pp. T26 7C.
- Schmidt, M., van Albada, S., Bakker, R., & Diesmann, M. (2014). A spiking multi-area network model of macaque visual cortex. In *2014 Neuroscience Meeting Planner. Washington, DC: Society for Neuroscience.*, pp. 186.22/TT43.
- Schmitt, O., Eipert, P., Kettlitz, R., Leßmann, F., & Wree, A. (2014). The connectome of the basal ganglia. *Brain Structure and Function*, 1–62.
- Seltzer, B., & Pandya, D. N. (1991). Post-rolandic cortical projections of the superior temporal sulcus in the rhesus monkey. *Journal of Comparative Neurology* *312*(4), 625–640.
- Seltzer, B., & Pandya, D. N. (1994). Parietal, temporal, and occipital projections to cortex of the superior temporal sulcus in the rhesus monkey: A retrograde tracer study. *Journal of Comparative Neurology* *343*(3), 445–463.
- Shen, K., Hutchison, R. M., Bezgin, G., Everling, S., & McIntosh, A. R. (2015). Network structure shapes spontaneous functional connectivity dynamics. *The Journal of Neuroscience* *35*(14), 5579–5588.
- Stephan, K., Kamper, L., Bozkurt, A., Burns, G., Young, M., & Kötter, R. (2001). Advanced database methodology for the collation of connectivity data on the macaque brain (cocomac). *Philosophical Transactions of the Royal Society London, Series B* *356*, 1159–1186.
- Stephan, M., & Docter, J. (2015). Juqueen: Ibm blue gene/q® supercomputer system at the jülich supercomputing centre. *Journal of large-scale research facilities JLSRF* *1*, 1.
- Strogatz, S. H. (1994). *Nonlinear Dynamics and Chaos: with Applications to Physics, Biology, Chemistry, and Engineering*. Reading, Massachusetts: Perseus Books.
- Suzuki, W. L., & Amaral, D. G. (1994). Perirhinal and parahippocampal cortices of the macaque monkey: cortical afferents. *Journal of comparative neurology* *350*(4), 497–533.
- Swadlow, H. A. (1988). Efferent neurons and suspected interneurons in binocular visual cortex of the awake rabbit: Receptive fields and binocular properties. *J. Neurophysiol.* *59*(4), 1162–1187.
- Tomioka, R., & Rockland, K. S. (2007). Long-distance corticocortical gabaergic neurons in the adult monkey white and gray matter. *Journal of Comparative Neurology* *505*(5), 526–538.
- Trousdale, J., Hu, Y., Shea-Brown, E., & Josic, K. (2012). Impact of network structure and cellular response on spike time correlations. *PLoS Comput. Biol.* *8*(3), e1002408.
- Turrigiano, G. G., Leslie, K. R., Desai, N. S., Rutherford, L. C., & Nelson, S. B. (1998). Activity-dependent scaling of quantal amplitude in neocortical neurons. *Nature* *391*, 892–896.
- van Albada, S., Helias, M., & Diesmann, M. (2015). Scalability of asynchronous networks is limited by one-to-one mapping between effective connectivity and correlations. *PLoS Comput. Biol.* *11*(9), e1004490.
- Van Essen, D. C. (2002). Windows on the brain: the emerging role of atlases and databases in neuroscience. *Current opinion in neurobiology* *12*(5), 574–579.

- Van Essen, D. C., Drury, H. A., Dickson, J., Harwell, J., Hanlon, D., & Anderson, C. H. (2001). An integrated software suite for surface-based analyses of cerebral cortex. *Journal of the American Medical Informatics Association* 8(5), 443–459.
- van Kerkoerle, T., Self, M. W., Dagnino, B., Gariel-Mathis, M.-A., Poort, J., van der Togt, C., & Roelfsema, P. R. (2014). Alpha and gamma oscillations characterize feedback and feedforward processing in monkey visual cortex. *Proc. Natl. Acad. Sci. USA* 111(40), 14332–14341.
- van Vreeswijk, C., & Sompolinsky, H. (1996). Chaos in neuronal networks with balanced excitatory and inhibitory activity. *Science* 274, 1724–1726.
- Voorhees, E. M. (1986). Implementing agglomerative hierarchic clustering algorithms for use in document retrieval. *Information Processing & Management* 22(6), 465–476.
- Wedeen, V. J., Wang, R., Schmahmann, J. D., Benner, T., Tseng, W., Dai, G., Pandya, D., Hagmann, P., D’Arceuil, H., & de Crespigny, A. J. (2008). Diffusion spectrum magnetic resonance imaging (ds) tractography of crossing fibers. *Neuroimage* 41(4), 1267–1277.
- Wong, K.-F., & Wang, X.-J. (2006). A recurrent network mechanism of time integration in perceptual decisions. *J. Neurosci.* 26(4), 1314–1328.